Post-critical *SsPmp* and Its Applications to Virtual Deep Seismic Sounding (VDSS) 1. Sensitivity to Lithospheric 1D and 2D Structure

Tianze Liu[1] (tianze@stanford.edu), Simon L. Klemperer[1], Chunquan Yu[2], Jieyuan Ning[3]
1. Department of Geophysics, Stanford University
2. Seismological Laboratory, California Institute of Technology
3. Institute of Theoretical and Applied Geophysics, School of Earth and Space Science, Peking University

Key words: Seismology, body waves, teleseismic imaging, crustal imaging, crustal structure, lithospheric imaging, lithospheric structure, Virtual Deep Seismic Sounding

Abstract

Virtual Deep Seismic Sounding (VDSS) has recently emerged as a novel method to image the Moho and potentially other lithospheric boundaries. The behavior of *SsPmp*, the post-critical reflection phase at the Moho that is utilized in VDSS, is rich with complexities not yet widely utilized. Here, motivated by observations from the Ordos Plateau in North China, we use synthetic seismograms computed with a broad range of models to evaluate how different parts of the lithosphere along the ray path of *SsPmp* affect its phase, amplitude, and arrival time. If the crust-mantle boundary is a sharp discontinuity, the *SsPmp* phase shift relative to the direct S wave varies from ~180º to ~ 0º with increasing values of lower-crustal V_p, upper-mantle V_p and ray parameter. This property indicates the possibility of using *SsPmp* to constrain V_p in the lower crust and uppermost mantle. If the crust-mantle boundary is a velocity-gradient zone with thickness smaller than the dominant wavelength of the converted P wave (~25 km), the *SsPmp* phase and amplitude do not differ significantly from the case with a discontinuity that has the same velocity increase. However, in such cases *SsPmp* arrival times vary as different functions of ray parameter from the cases with sharp crust-mantle boundary, because different rays turn at different depths, allowing measurement of the vertical velocity gradient in the crust-mantle transition zone. If the virtual source (location of S-to-P conversion at the free surface) is in a sedimentary basin, *SsPmp* amplitude can be significantly reduced due to low S-to-P reflected energy at the virtual source. This may cause the absence of *SsPmp* despite appropriate source-receiver geometry. The *SsPmp* arrival time relative to direct S is not only controlled by crustal thickness at the reflection point, but also by lateral variation of V_s beneath the virtual source and the receiver. The accuracy of crustal-thickness measurements from *SsPmp* arrival times thus

depends on our knowledge of the variability of lithospheric V_s and crustal V_p across a broad region.

1. Introduction

For a quarter-century the seismic community has relied heavily on receiver function (RF) techniques, which use teleseismic P-to-S (*Pms* or PRF) or S-to-P (*Smp* or SRF) conversion phases, to image discontinuities in the lithosphere (Fig. 1) (e.g. Kind et al., 1995; Langston, 1979; Owens and Taylor, 1984). In recent years, Virtual Deep Seismic Sounding (VDSS) has emerged as a novel method to image the crust-mantle boundary (CMB) and has been successfully applied to multiple datasets from different areas as a complement to RF techniques (e.g. Kang et al., 2016; Parker et al., 2016; Tseng et al., 2009; Yu et al., 2016, 2012). Here we use *CMB* to denote the geological transition from crust to mantle, whether abrupt or a "velocity-gradient zone" spanning many kilometers; and *Moho* to denote a seismological inference about this transition, typically given as single depth. *SsPmp*, the seismic phase used in VDSS, originates when upcoming teleseismic S waves convert to down-going P waves at the free surface (the virtual source), which then undergo post-critical reflection at or within the CMB and finally reach the receiver (Fig. 1). The arrival time of *SsPmp* relative to the direct S arrival (or *Ss*), hereafter T_{VDSS}, is used to estimate the Moho depth at the reflection point, normally assumed to be the midpoint between the virtual source and receiver. Because VDSS uses teleseismic events, the incident S wave can be approximated as a plane wave with constant ray parameter. To enable post-critical reflection of *SsPmp* at the Moho, appropriate epicentral distances are ~40–50º, corresponding to ray parameter p = ~0.1256–0.1345 s/km for a focal depth of 0 km ($1/p$ = ~7.96–7.43 km/s), and slightly smaller p for larger focal depths (Fig. 2). Due to post-critical reflection at the Moho, *SsPmp* usually has amplitude comparable to *Ss* (Fig. 3a), making it possible to construct a seismic profile with a single event recorded by an array (Figs. 4b,c). Because *SsPmp* undergoes post-critical reflection at the Moho, its phase is changed relative to *Ss* (e.g. Aki and Richards, 1980) (Fig. 3a; hereafter referred to as phase shift for simplicity and denoted Φ_{VDSS}), making it difficult to directly pick T_{VDSS} from raw records. Previous studies (e.g. Tian et al., 2015; Tseng et

al., 2009; Yu et al., 2016;) have used 1D waveform fitting to measure T_{VDSS}, and then find the trade-off relation between crustal V_p and thickness H using the equation:

$$T_{VDSS} = 2H\sqrt{\frac{1}{V_p^2} - p^2} \qquad (1)$$

where p is the ray parameter of the incident waves. In the process of waveform fitting, the upper mantle has commonly been assumed to be a half space and its V_p (or V_p^{um}) has been fixed based on *a priori* knowledge of V_p^{um} of the study area due to the recognized effect of V_p^{um} on *SsPmp* waveforms (e.g. Tian et al., 2015; Yu et al., 2016). Similarly, previous VDSS studies have commonly assumed for the purposes of waveform fitting that the CMB is a discontinuity at which V_p jumps from typical crustal values (~6.5 km/s) to typical upper mantle values (~8.1 km/s). Tseng et al. (2009) and Yu et al. (2012) discussed the case in which the CMB is a velocity gradient zone and showed that the *SsPmp* waveforms appeared similar to the case in which the CMB is a discontinuity. Multiples (reverberations) generated in sedimentary basins severely contaminate receiver-function waveforms and have presented a long-standing challenge to the utility of receiver functions (e.g. Bao and Niu, 2017; Guan and Niu, 2017; Langston, 2011; Tao et al., 2014; Yu et al., 2015). In contrast, the manner in which sedimentary basins affect *SsPmp* waveforms is not widely understood. Parker et al., 2016 showed that *SsPmp* responds differently to a vertically homogeneous basin and to a basin with velocity increasing downward.

Here we present as motivation a dataset from the Ordos Plateau in North China in which significant changes in *SsPmp* phase shift, amplitude relative to direct S, and travel time delay (Φ_{VDSS}, A_{VDSS}, T_{VDSS}) are observed across the recording array. We first use synthetic waveforms to demonstrate that, when the CMB is a sharp discontinuity, Φ_{VDSS} decreases from ~180º to ~ 0º as the lower crustal V_p (hereafter V_p^{lc}) or upper mantle V_p (hereafter V_p^{um}) or ray parameter p increases. Additionally, when p is small ($1/p$ is close to V_p^{um}) Φ_{VDSS} is more sensitive to V_p^{um} than V_p^{lc}, whereas when p is large ($1/p$ is close to V_p^{lc}) Φ_{VDSS} is more sensitive to V_p^{um} than V_p^{um}. We next show that when the CMB is a velocity gradient zone with thickness up to the dominant wavelength of incident S wave (*Ss*), neither Φ_{VDSS} nor A_{VDSS} varies significantly with p, but T_{VDSS} varies as different functions of p from the case with sharp CMB, because rays with different ray parameters turn at different depths within the velocity-gradient zone. This feature should make VDSS an ideal method to study CMB structure in areas such as the Colorado Plateau, where a

sharp Moho is not observed by traditional methods based on pre-critical reflections and conversions (Hauser and Lundy, 1989; Shen et al., 2013). We also demonstrate that although A_{VDSS} is largely insensitive to CMB structure, A_{VDSS} is significantly decreased by low near-surface velocity at the virtual source, which may explain cases of the absence of *SsPmp* from records with otherwise proper observation geometries. Finally, we use 2D synthetic seismograms to show that T_{VDSS} is affected not only by crustal thickness at the reflection point, but also by heterogeneity in V_s structure beneath the virtual source and receiver, for instance lateral variation in lithospheric thickness, which must be accounted for when using T_{VDSS} to estimate crustal thickness. Our analyses qualitatively explain the variation of Φ_{VDSS} and A_{VDSS} in our example from the Ordos Plateau. In our companion paper (Liu et al., unpublished manuscript, hereafter "Part 2"), we quantitatively analyze a more comprehensive dataset from the Ordos Plateau in order to demonstrate the use of post-critical *SsPmp* in imaging lithospheric structure.

2. Data

The Ordos Plateau in northern China (Fig. 3c) is a site of considerable interest, as it is the surviving remnant of the Archean North China Craton (Liu et al., 1992). It is unknown why this region preserved its lithospheric root while the eastern part of the craton underwent significant modification (decratonization) in Mesozoic time (Gao et al., 2008; Griffin et al., 1998; Menzies et al., 1993). To study the lithospheric structure of the Ordos Plateau, a W–E linear seismic array was deployed across the Ordos Plateau at ~37.5º N during 2006-2008 by Peking University (Yu et al., 2012), and recorded abundant intermediate to deep seismicity in the west-Pacific subduction zones at epicentral distances of 40–50º, making the dataset ideal for observing post-critical *SsPmp* (Fig. 4a). Because the western and eastern parts of the array were deployed in two different time periods, we use two nearby events (~400 km separation) in the Banda Sea to make a single record section (Figs. 4b,c). The traces are bandpass filtered from 0.04 – 0.5 Hz, separated into pseudo-P (motion associated with incoming P waves) and pseudo-SV (motion associated with incoming SV waves) components (hereafter referred to as P and S for simplicity) with a particle-motion analysis algorithm (Yu et al., 2013), aligned along their direct S (*Ss*) arrival times. The *Ss* arrival times are picked at the zero-crossings of the *Ss* wavelets, which closely resemble a first-order Hermitian wavelet (first derivative of Gaussian wavelet; Figs. 4b-f), because for a first-order Hermitian wavelet the peak of its envelope function is at its zero-

crossing and does not change after an arbitrary phase shift. The sensitivity of measured arrival time to the addition of noise could make the use of the zero-crossing less appropriate for real data than for these synthetics. Our synthetic waveforms are normalized to the peak amplitudes of the corresponding direct S arrivals.

We observe significant variation in A_{VDSS} across the array. For instance, A_{VDSS} of JB09 is only about half of JB13 (Figs. 4d,e), despite a station separation of only ~60km. Because the traces are normalized by the peak amplitudes of *Ss*, the effects of source radiation pattern are removed (and should anyway be minor since the aperture of the array is small compared to the epicentral distance). The rapid change of A_{VDSS} across the array thus must be due to structure near the stations. Φ_{VDSS} also varies rapidly across the array. At JB13, *SsPmp* has a ~90º phase advance relative to *Ss* (Fig. 4e), as commonly assumed for post-critical *SsPmp* (Tseng et al., 2009). However, only ~120-km distant, at FY03 the *SsPmp* waveform closely resembles *Ss*, indicating a ~ 0º phase shift (Fig. 4f). Φ_{VDSS} is unrelated to the source and should be primarily controlled by structure close to the stations. A_{VDSS} and Φ_{VDSS} are crucial properties that need to be correctly modeled in order to measure T_{VDSS}. If the signal-to-noise ratio of *SsPmp* is very small, it will be difficult to measure its arrival time. Even when *SsPmp* amplitude is high, as for JB13 and FY03, improperly modeling the phase of *SsPmp* will cause up to ~1s error in T_{VDSS}, which corresponds to ~5 km error in the resulting crustal thickness estimation, a nontrivial error in most applications. The phenomenon of significant spatial variation of A_{VDSS} and Φ_{VDSS} has not been systematically explored by previous studies. Another unexpected feature of the Ordos dataset is that T_{VDSS} varies significantly across the array (Fig. 4a). Using the arrival time of the strongest peaks on the P component as an approximation of T_{VDSS} (equivalent to assuming a 90º phase shift), we find that T_{VDSS} reaches its maximum of ~12 s at ~110.5º E, nominally corresponding to a crustal thickness of ~60 km, and then decreases rapidly eastward, reaching ~6 s at ~113º E, which corresponds to a crustal thickness of ~30 km (Yu et al., 2012). This change in travel-time is far greater than possible phase delays that are limited to 0–180°, or ~2 s for these ~4 s period arrivals. The unexpectedly deep Moho was previously interpreted as preservation of a ~20-km thick, mafic lower-crustal layer beneath the Ordos Plateau, relict from craton formation (Yu et al., 2012). However, the recent recognition that lateral variation in V_s structure affects T_{VDSS} (Yu et al., 2016) makes the direct relation of T_{VDSS} to crustal thickness problematic. Therefore, it is important to evaluate quantitatively how realistic lateral variations of V_s affect T_{VDSS}. In the

following sections, we use synthetic seismograms to examine possible lithospheric structures that may affect A_{VDSS}, Φ_{VDSS} and T_{VDSS}.

3. Synthetic Tests

3.1. Sensitivity to V_p across the crust-mantle boundary (CMB)

In this section, we first assume that the lithosphere consists of three homogeneous layers separated by abrupt discontinuities: the upper crust, lower crust and upper mantle (Figs. 5a, 6a). The *SsPmp* waveform is affected by V_p of the lower crust and upper mantle, therefore we first vary V_p^{lc} with fixed V_p^{um} (Fig. 5a), and then vary V_p^{um} with V_p^{lc} fixed (Fig. 6a), to test the sensitivity of the *SsPmp* waveform to the two parameters. As V_p varies, we vary V_s to keep Poisson's ratio constant at 0.25, and vary density to satisfy the Nafe-Drake relation (Brocher, 2005). We compute waveforms using the reflectivity algorithm in a layered medium (Randall, 1989), in which the incident S wave has a constant ray parameter p = 0.127 s/km ($1/p$ = 7.87 km/s). The source time function is assumed to be a first-order Hermitian wavelet (first derivative of a Gaussian wavelet) with a half width of ~2 s, which has similar shape and frequency to observed *Ss* of deep or intermediate-depth earthquakes (Fig. 3).

Fig. 5b shows synthetic seismograms computed with V_p^{lc} ranging from 7.0–7.8 km/s and V_p^{um} fixed at 8.0 km/s. This range of V_p^{lc} is characteristic of continental lower crust made of predominantly mafic rocks (Christensen and Mooney, 1995). As V_p^{lc} increases, *SsPmp* arrives earlier (T_{VDSS} decreases) and becomes closer to the reflection phase at the top of the lower crust (*SsPip* with *i* standing for intra-crustal interface; Fig. 5b), with little change in A_{VDSS} and Φ_{VDSS} (Fig. 5d). The amplitude of *SsPip* grows as V_p^{lc} increases (Fig. 5c), interfering with *SsPmp* and distorting its waveform (Fig. 5b). The different responses of *SsPip* and *SsPmp* to velocity changes indicate their different natures. As a pre-critical reflection, the amplitude of *SsPip* grows as the velocity contrast at the intra-crustal interface increases. In contrast, as a post-critical reflection phase, the amplitude of *SsPmp* (A_{VDSS}) stays constant despite changes of velocity contrast across the Moho, because all incident energy is reflected upwards at the CMB (V_p^{um} exceeds the ray parameter p).

Fig. 6 shows the sensitivity of *SsPmp* waveforms to V_p^{um}. We compute synthetic seismograms using models with V_p^{um} ranging from 7.9–8.5 km/s and V_p^{lc} fixed at 7.0 km/s (Fig.

6a). The range of V_p^{um} used here covers most of the observed range for the continental uppermost mantle (Christensen and Mooney, 1995), and also ensures post-critical reflection of *SsPmp* at the CMB for our chosen ray parameter (1/p=7.87 km/s). Our synthetic seismograms show the strong dependence of Φ_{VDSS} on V_p^{um} (Fig. 6b). When V_p^{um} = 7.9 km/s, Φ_{VDSS} is close to 180º (corresponding to the source wavelet multiplied by -1), and the waveform is very similar to the pre-critical reflection. As V_p^{um} increases, Φ_{VDSS} first decreases to ~90º, and then further drops towards 0º (Fig. 6b). Another important observation is that despite the significant change in phase, A_{VDSS} stays the same as V_p^{um} increases, because all incident energy is post-critically reflected. Because Φ_{VDSS} (the *SsPmp* waveform) is sensitive to V_p^{um}, one must know V_p^{um} in order to correctly measure T_{VDSS}. An example is shown in Fig. 6c, in which we assume the *SsPmp* wavelet to be phase-shifted by 90º from *Ss*, and cross-correlate it with synthetic waveforms computed with models in Fig. 6a in order to find T_{VDSS}. The resulting T_{VDSS} for each model is then converted to estimated crustal thickness (Moho depth) using Eq. 1 with the true average crustal V_p. We observe that a 90º phase shift is only a good approximation when V_p^{um} = 8.3 km/s, whereas for V_p^{um} = 7.9 km/s the estimated Moho depth is ~5 km larger than the true value (Fig. 6c). This example highlights the importance of using the correct V_p^{um} in measuring T_{VDSS} and estimating Moho depth.

To explore the effect of ray parameter p on Φ_{VDSS} and its sensitivity to V_p^{lc} and V_p^{um}, we calculate Φ_{VDSS} as functions of V_p^{lc} and V_p^{um} for p = 0.127 and 0.130 s/km. When p = 0.127 s/km (1/p = 7.87 km/s), Φ_{VDSS} is largely controlled by V_p^{um} (Fig. 7a; also Figs. 5, 6). However, when p = 0.130 s/km (1/p = 7.69 km/s), Φ_{VDSS} depends more on V_p^{lc} than V_p^{um} (Fig. 7b). Besides, Φ_{VDSS} decreases for all V_p^{lc} and V_p^{um} when p increases from 0.127 s/km to 0.130 s/km (Fig. 7). This example indicates that increasing p not only reduces Φ_{VDSS}, but also makes Φ_{VDSS} more sensitive to V_p^{lc} and less sensitive to V_p^{um}. Combining the above examples, we conclude that increasing V_p^{lc}, V_p^{um} and p decreases Φ_{VDSS}, and that when p is small (1/ p is close to V_p^{um}) Φ_{VDSS} is more sensitive to V_p^{um} than V_p^{lc}, whereas when p is large (1/ p is close to V_p^{lc}) Φ_{VDSS} is more sensitive to V_p^{lc} than V_p^{um}.

3.2. Sensitivity to CMB Thickness

To understand how CMB thickness affects *SsPmp* waveforms, we model the CMB as a transition from V_p = 6.5 km/s, typical of crustal rocks, to V_p = 8.1 km/s, typical of uppermost-mantle rocks. As before, V_s and density are varied simultaneously with V_p to keep Poisson's ratio at 0.25 and to satisfy the Nafe-Drake relation (Brocher, 2005). We model the transition zone as a stack of 1-km-thick layers and vary the transition thickness from 0–20 km below a fixed top at 40 km (Fig. 8a). As the CMB becomes thicker, there is little change in either A_{VDSS} or Φ_{VDSS} (Fig. 8b). This behavior is distinct from that of pre-critical reflected and converted phases at the CMB, which become broader and weaker as the CMB thickens. The clear change in Fig. 8b is that T_{VDSS} becomes larger as the post-critical reflection occurs at greater depth, because in each case the incident wave turns at the depth within the CMB where $V_p = 1/p$, so the turning depth becomes larger as the CMB thickness increases (Fig. 8a).

Fig. 9 compares the responses of PRF and VDSS to different CMB thicknesses (Figs. 9a,b). The model in Fig. 9b is identical to the model with a 20-km-thick CMB in Fig. 8a, whereas Fig. 9a is the 0-km-thick CMB model in Fig. 8a with the discontinuity shifted from 40 km to 50 km, so that the centers of the CMBs are at the same depth in Fig. 9a and b. When the incident waves are plane P waves with ray parameters in the range 0.04-0.08 s/km, the computed PRFs are strong and narrow for a discontinuous CMB (Fig. 9c), but broad and weak for a transitional CMB (Fig. 9d) (even the strongest *Pms* on the PRFs shown here is only ~20% the amplitude of the first arrival). As the CMB thickens, high-frequency components of the incident P waves with wavelengths shorter than the scale of the CMB become insensitive to it, eliminating high-frequency components of *Pms*. The *Pms* waveforms stay unchanged as the ray parameter varies from 0.04-0.08 s/km for both a sharp CMB (Fig. 9c) and a broad CMB (Fig. 9d). Theoretical *Pms* arrival times (calculated assuming that conversion occurs at the center of the CMB) closely match the centers of observed *Pms*, and are very similar at the same ray parameter, for both sharp and broad CMBs (Figs. 9c,d). The above behaviors would also be observed for pre-critical *Pmp* and *SsPmp* reflections.

In contrast, post-critical *SsPmp* is a strong phase whether the CMB is a discontinuity or a broad transition zone, and has similar amplitude to *Ss* (Figs. 9f, 8b). The reason that post-critical *SsPmp* remains strong as the CMB thickens is that all frequency components of the down-going P wave are reflected (or turned) at the depth where, for that ray parameter, V_p reaches the critical velocity. As a result, T_{VDSS} predicted using the reflection depth as the depth where the critical

velocity is reached follows the move-out of *SsPmp* closely in the transitional model (Fig. 9f) but differs significantly from T_{VDSS} in the sharp CMB case (Fig. 9e).

When an incident plane wave turns in a medium with positive vertical velocity gradient, the turning wave will have a 90º phase shift relative to the incident wavelet (Shearer, 1999). However, our synthetic waveforms show that, for CMB thickness < 20 km, Φ_{VDSS} of the transitional models are similar to the discontinuity model with the same p (Figs. 8b, 9e,f), instead of 90º. The reason is that the dominant wavelength of down-going P wave in the CMB (~25 km for a dominant frequency of ~0.25 Hz) is similar to the CMB thickness (< 20 km), causing Φ_{VDSS} to be insensitive to the presence of the transition zone. Since the transitional models have the same total velocity increase across the CMB as the discontinuity model, Φ_{VDSS} of the transitional models are similar to the discontinuity model at a given p. To further test our hypothesis, we computed Φ_{VDSS} for CMB thicknesses up to 60 km with the total velocity increase across the CMB the same as the discontinuity model (Fig. 8c). The results show that as CMB thickness exceeds ~20 km, Φ_{VDSS} starts to deviate significantly from the discontinuity model (Φ_{VDSS} = 119º), and gradually approaches 90º as CMB thickness further increases (Fig. 8c). This supports our hypothesis that Φ_{VDSS} is similar in both transitional and discontinuity models due to finite-frequency effects. In principal, higher-frequency incident waves would show a more pronounced difference between Φ_{VDSS} produced by a sharp and a broad CMB, though recorded teleseismic S waves seldom have energy above 1 Hz. Therefore, we conclude that, for CMB thickness smaller than ~25 km, no significant difference exists between Φ_{VDSS} caused by a sharp CMB and by a broad CMB, though the two models cause distinct move-out of T_{VDSS} with p (Fig. 9f).

3.3. Sensitivity to Sedimentary Basins

In the presence of sedimentary basins, we expect the waveforms of *SsPmp* to be affected by the thickness, velocity, Poisson's ratio (or V_p/V_s ratio), and velocity gradient of the sedimentary layer. We next test the sensitivity of *SsPmp* waveforms to sedimentary basins by varying each of these four parameters, one at a time (Figs. 10a-d). Our reference basin model is a homogeneous layer with V_p = 4.5 km/s, Poisson's ratio = 0.25, and thickness = 6 km. For simplicity, we assume the basin has uniform properties both at the virtual source and at the receiver (Fig. 10j).

3.3.1. Sedimentary-layer thickness

To test the effects of sedimentary-layer thickness on *SsPmp* waveforms, we vary thickness from 0 km (bed-rock case), 3 km (shallow-basin) to 6 km (deep-basin) (Fig. 10a). Both basin cases have similar A_{VDSS}, clearly lower than the bed-rock case (Fig. 10e). *SsPmp* arrives increasingly later (T_{VDSS} increases) as the basin becomes deeper, because the basin has lower velocities than the bed rock (Fig. 10e). Also visible in the two basin cases are the seismic arrivals *Sbp* (S-to-P conversion phase at the basin-basement interface *b*) and *SsPbp* (pre-critical P reflection phase at the basin-basement interface after S-to-P reflection at the free surface) (Fig. 10e), both delayed slightly from *Ss*. As the basin becomes thicker, *Sbp* and *SsPbp* are increasingly delayed from *Ss* (Fig. 10e). *SsbPmp* (S-to-P reflection at the basin-basement interface followed by post-critical reflection at the Moho) is not observed because the velocity contrast at the basin-basement interface is not large enough to generate strong S-to-P reflections (Fig. 10e).

The reduced A_{VDSS} in the presence of sedimentary cover has profound significance, as none of the parameters previously examined (V_p^{lc}, V_p^{um} and CMB thickness) have significant effects on A_{VDSS}, thus cannot explain observations of highly variable *SsPmp* amplitude (Figs. 4d,e). We interpret the low *SsPmp* amplitude in the presence of a sedimentary basin as caused by the low V_s at the virtual source, which reduces the incident angle of the incoming S wave at the free surface and lowers the reflection coefficient between the incident S wave and reflected P wave. (In an extreme case, a vertically incident S wave produces no reflected P wave.) Because it is the reflected P wave at the free surface that is later reflected at the Moho to form *SsPmp*, the sedimentary layer reduces A_{VDSS}. In other words, the "efficiency" of the virtual source decreases due to the sedimentary basin at the virtual source. Because the dominant wavelength of the incident S wave is ~10 km in the sedimentary layer, significantly larger than 3 and 6 km, the increase of basin thickness from 3 to 6 km does not profoundly increase the affected spectrum. Therefore, A_{VDSS} does not vary significantly when the basin deepens from 3 to 6 km (Fig. 10e).

3.3.2. Sedimentary-layer velocities

To test the effects of sedimentary-layer velocities on *SsPmp* waveforms, we vary V_p in our homogeneous basin from 4.5 km/s (high-V_p case), 3.5 km/s (intermediate-V_p), to 2.5 km/s (low-V_p case) (Fig. 10b). Because we hold the Poisson's ratio constant, V_s of the basin changes accordingly. As sedimentary V_p drops, we observe a dramatic decrease in *SsPmp* amplitude (Fig. 10f). In the high-V_p case *SsPmp* is still the dominant phase, whereas in the intermediate and low-

V_p cases A_{VDSS} becomes so low that it is hard to distinguish it from other basin phases (Fig. 10f). Another important observation is that in the low-V_p case a strong P phase arrives at ~4.5 s, ~5 s earlier than predicted T_{VDSS} (Fig. 10f), and could be easily misinterpreted as *SsPmp* due to its high amplitude. We interpret this strong P arrival as a superposition of *SsPbp* and *SsbPmp* that arrive at approximately the same time. As the velocity contrast at the basin-basement interface increases, the S-to-P reflection at the interface becomes stronger, further increasing *SsbPmp* amplitude. If we increase the CMB depth to 60 km, the temporal separation between *SsPbp* and *SsbPmp* will increase so that they appear as two distinct arrivals (Fig. S1), thereby supporting our interpretation that the strong P phase at ~4.5s in the low-V_p case is the superposition of *SsPbp* and *SsbPmp*. In summary, when basin velocity is relatively low and basin thickness is large enough (dominant frequency component of the incident wave is sensitive to the basin), *SsPbp* and *SsbPmp* become the dominant P phases and can be easily misidentified as *SsPmp*, which may cause significant errors in Moho depths inferred from T_{VDSS}.

The above examples show that *SsPmp* amplitude is strongly controlled by basin velocity (Figs. 10a-f), which we interpret as a result of reduced S-to-P reflection coefficient at the virtual source in the presence of sedimentary basins. To further validate our interpretation, we calculate the maximum amplitude in a 4-s time window around the theoretical T_{VDSS} as a proxy for A_{VDSS} for models with basin V_s varied from 1.45-3.75 km/s (sedimentary-layer thickness and Poisson's ratio remain fixed at 6 km and 0.25) (Fig. 10i). We also calculate the S-to-P reflection coefficient at the free surface for a half-space (i.e. no basin) for the same V_s range and Poisson's ratio = 0.25 (Fig. 10i). A comparison of the two values shows near equivalence for $V_s > 2.25$ km/s, suggesting the S-to-P reflection ratio is a primary control on A_{VDSS} (Fig. 10i). As V_s decreases from 2.15–2.05 km/s, A_{VDSS} drops faster than the S-to-P reflection ratio probably due to interference with other sedimentary phases, but for $V_s < 2.05$ km/s, *SsPmp* amplitude again decreases at about the same rate as S-to-P reflection ratio (Fig. 10i). Other factors causing the small discrepancy between A_{VDSS} and S-to-P reflection ratio likely include transmission loss at the basin-basement interface and finite-frequency effects.

3.3.3. Sedimentary-layer *Vp*/*Vs*

To test the effects of sedimentary Poisson's ratio on *SsPmp* waveforms, we vary Poisson's ratio from 0.25, 0.275 to 0.3 (Fig. 9c). Increasing Poisson's ratio ν corresponds to increasing V_p/V_s ratio as:

$$V_p/V_s = \sqrt{\frac{2(1-\nu)}{1-2\nu}} \qquad (2)$$

Because we hold basin V_p constant, increasing Poisson's ratio causes basin V_s, thus S-wave incident angle, to decrease. Therefore, the amplitude of *SsPmp* decreases with increasing sedimentary Poisson's ratio (Fig. 10g). Although the range of Poisson's ratio used here is quite large and covers most sedimentary rocks (Brocher, 2005), the effect of basin Poisson's ratio on A_{VDSS} is quite limited (Fig 10g). Because T_{VDSS} is only related to V_p in the crust (Eq. 1), despite changes of A_{VDSS}, *SsPmp* arrive at identical times in all three cases (Fig. 10g).

3.3.4 Sedimentary-layer velocity gradient

To test how vertical velocity gradient in sedimentary basins affects *SsPmp* waveforms, we compare results for a constant-velocity basin (homogeneous case) with results from a basin formed of six 1-km-thick layers with velocity linearly increasing from 2.5 km/s at the surface to 6.5 km/s at the basin-basement interface (gradient case) (Fig. 10d). Although the basins in both cases have the same average velocity, our synthetic seismograms show that A_{VDSS} is further reduced in the gradient case (Fig. 10h). This is because the multiple sub-layers strongly scatter short-wavelength components of incident *Ss* (both forward and backward), while the long-wavelength components of the incident S wave only respond to the average properties of the basin that are the same as in the homogeneous case. As the result of normal S-to-P reflection ratio for long-wavelength components but reduced S-to-P reflection ratio for short-wavelength components at the virtual source, *SsPmp* in the gradient case is depleted in high frequencies and has lower amplitude than *SsPmp* for the homogeneous case (Fig. 10h). Because sedimentary basins commonly have velocities increasing with depth, this example explains why in some cases observed A_{VDSS} can be even lower than A_{VDSS} predicted for homogeneous sedimentary layers.

3.4. Sensitivity to Lateral Heterogeneity in the Mantle

Yu et al. (2016) discussed the effects of local-scale lateral heterogeneity in the crust and the uppermost mantle (i.e. deviations from 1D Earth models) that causes travel-time differences between up-going S legs of *SsPmp* and *Ss*, thereby causing significant errors in interpretations of T_{VDSS} using 1D assumptions (Eq. 1). A simple example would be the juxtaposition of thick Archean lithosphere (>200 km) and Phanerozoic lithosphere of normal thickness (~80 km),

putatively the case at the boundaries of the Ordos Block (Fig. 4) (Yu et al., 2012). We would like to quantify the effects of such lateral heterogeneity on *SsPmp* waveforms.

We create a 2D model with a constant crustal thickness of 40 km, in order to explore only the effect of mantle heterogeneity on *SsPmp* waveforms (Fig. 11a). The lithosphere comprising both the crust and lithospheric mantle is 80-km thick at each end, and 200-km thick in the center of the model. The 200-km thick lithosphere linearly shallows to 80 km across 200 km, forming two straight ramps dipping at 31° (Fig. 11a). The velocity of the lithospheric mantle is ~5% faster than the asthenosphere (Fischer et al., 2010). We use the SPECFEM2D software package to compute the surface-recorded seismograms of a plane S wave with ray parameter 0.1275 s/km (incident angle of 35º in the asthenosphere) incident on the bottom-left of the model (Komatitsch et al., 2001; Komatitsch and Vilotte, 1998; Tromp et al., 2008). Despite a constant crustal thickness in our model, the synthetic seismograms show significant variation of T_{VDSS} across the recording array (Fig. 11b). On the far left of the array, where both virtual sources and receivers are located above thin lithosphere, *SsPmp* arrives at ~6.9 s (Fig. 11b), in agreement with the 1D prediction. When the receiver is located at the edge of the area with thick lithosphere (blue triangle in Fig. 11a), with the corresponding virtual source (blue star in Fig. 11a) above thinner lithosphere, T_{VDSS} increases to ~8 s, significantly later than the 1D prediction (blue traces in Figs. 11b,c). In the center of the area with thick lithosphere, where receivers and corresponding virtual sources are both in areas with thick lithosphere, observed T_{VDSS} returns to the time predicted for the 1D model (black virtual source, receiver, traces in Figs. 11a-c). At the right edge of the area with thick lithosphere, where the receivers are located above thinner lithosphere than their virtual sources, T_{VDSS} rapidly decreases to ~5.5 s, significantly earlier than the 1D prediction (red triangle, star and traces in Figs. 11a-c). If this observed T_{VDSS} is used to infer crustal thickness with an 1D assumption, the 1.5 s difference from the theoretical T_{VDSS} will cause ~9 km error in Moho depth! The explanation for the anomalous T_{VDSS} is that when the up-going S wave leg of *Ss* travels through a velocity anomaly that is not present on the path of *SsPmp* (Fig. 11d), the travel-time difference between the two ray paths deviate from predictions made by assuming 1D Earth structure, and the residual will be included in the observed T_{VDSS}. Therefore, when applying VDSS to data collected in areas with significant variation in lithosphere thickness, it is vital to correct for S travel-time residuals before converting observed T_{VDSS} to crustal thickness. A practical approach to this correction is presented in Part 2.

Another interesting feature of our synthetic seismograms is that the *Ss* observed above the right margin of the thick lithosphere is significantly stronger than that observed along the rest of the profile (red traces in Figs. 11b,c). The increase in *Ss* amplitude cannot be due to crustal structure as it is uniform along the profile. A probable explanation is that the lithosphere ramp on the right edge of the thick lithosphere causes energy to be focused (multi-pathing effect). Note that we apply no normalization to the traces in Figs. 10b,c. If the traces are normalized with the peak *Ss* amplitude of each trace, a common practice in VDSS data processing, the red trace at the right edge of thick lithosphere will have a low A_{VDSS} = 0.83 due to its high *Ss* amplitude. In contrast, the blue trace at the left edge of thick lithosphere (Fig 11a-c) will have A_{VDSS} = 1.23. Thus, lateral heterogeneity in the mantle can affect A_{VDSS}, as well as T_{VDSS}, by changing the energy distribution across the incident S wavefront.

4. Discussion

The nature of *SsPmp* as a post-critical, thus wide-angle, reflection phase brings both advantages and disadvantages in using T_{VDSS} to infer Moho depth. A clear advantage of *SsPmp* compared with narrow-angle phases (e.g. *Pms* used in PRF) is its high amplitude, which makes it possible to constrain crustal thickness with a single record. In addition, the long ray path of *SsPmp* in the crust causes T_{VDSS} to have a stronger dependence on ray parameter (or higher "move-out") than *Pms*, making it feasible to use the move-out of *SsPmp* to simultaneously constrain crustal thickness and crustal average V_p (Kang et al., 2016). In addition, given a uniform azimuthal distribution of earthquakes, it is possible to measure crustal thickness on a circle with ~60-km radius centered at the receiver, a much broader range than the CMB depth sampled by PRFs that is usually within 15 km from the receiver. Moreover, post-critical reflection causes a phase shift Φ_{VDSS} between *SsPmp* and *Ss*, which can be used to determine V_p^{lc} and V_p^{um}, though this inference requires particularly high-quality waveform data (see Part 2).

Disadvantages of the long crustal ray path of *SsPmp* include its sensitivity to lateral variation over a wide area, both in basins near the surface and at mantle depths. For instance, Fig. 10 shows that sedimentary basins at virtual sources can significantly reduce A_{VDSS}, making it difficult to measure T_{VDSS}. Sedimentary basins may also generate phases (*SsPbp*, *SsbPmp*, etc.) that are stronger than *SsPmp*, and can easily be misidentified as *SsPmp*, thus causing large errors in inferred Moho depths (Fig. 10) (though offering the ability to study basin structure). Dense 1D

or 2D arrays that cover both basins and adjacent exposed basement are key to avoiding such mistakes, because the gradual transition in waveforms allows recognition of sedimentary effects. In a second example, Fig. 11 shows the effect of heterogeneous mantle velocity structure on A_{VDSS} and T_{VDSS}, which can be partially overcome by application of "static" corrections given data collected by a dense 2D array (Yu et al., 2016). In general, future work using *SsPmp* to study crustal properties should leverage the power of dense arrays to alleviate challenges posed by its long ray path in the crust.

When the CMB is a transition zone, *SsPmp* is a turning wave with post-critical reflection at the depth where V_p reaches the critical velocity ($1/p$). Because *SsPmp* is high amplitude even for a transitional CMB, it is possible to use *SsPmp* with different ray parameters, which turn at different depths, to constrain the interior structure of the CMB (Fig. 9). In contrast, conversion phases such as *Pms* (and pre-critical reflection phases) may be too weak to image a transitional CMB. In areas with poorly-defined or absent PRF Moho, such as the Colorado Plateau, analysis of post-critical *SsPmp* may reveal more details of the CMB.

The Ordos Plateau is overlain by thick west-dipping Phanerozoic strata, with the age of exposed rocks decreasing westward (Xia et al., 2017; Yang et al., 2005). The virtual source of JB09 is west of the virtual source of JB13 (Fig. 4c), so is above younger, thus likely lower-velocity sedimentary rocks. A wide age range of sedimentary rocks may also cause significant velocity gradients across the basin. These factors may explain the significantly reduced A_{VDSS} at JB09 compared to JB13. In contrast to the change in A_{VDSS} between JB09 and JB13, the change in Φ_{VDSS} between JB13 and FY03 may have a more complicated origin. As shown in Figs. 5,6, elevated V_p^{lc} and V_p^{um} reduce Φ_{VDSS}, and may cause $\Phi_{VDSS} \approx 0^o$ at FY03. In addition, if the CMB is dipping from the virtual source towards the station, the incident angle of *SsPmp* at the Moho is increased, thus increasing ray parameter p and decreasing Φ_{VDSS} (Fig. 7). Because the virtual source of FY03 is closer than station JB13 to the actively extending Shanxi Graben System (Fig 4a), the crust at the virtual source is likely thinner than at the station, causing a dipping CMB that may also contribute to the very small Φ_{VDSS} at FY03. Quantitative analysis of change in A_{VDSS} and Φ_{VDSS} across the Ordos Plateau is beyond the scope of this paper and will be presented in detail in Part 2.

5. Conclusion

Using synthetic seismograms, we find that Φ_{VDSS} is negatively related to V_p^{lc}, V_p^{um} and p, making it possible to constrain V_p^{lc} and V_p^{um} with observed *SsPmp* waveforms. A_{VDSS} is insensitive to CMB thickness but is strongly affected by near-surface velocity at the virtual source. If the CMB is a velocity gradient zone, *SsPmp* is a turning wave within the CMB, with turning depth determined by the ray parameter, thereby offering the potential to image the CMB in areas where methods based on conversion and pre-critical reflection phases fail to show a clear Moho. We also show that T_{VDSS} is affected not only by crustal thickness, but also by crustal and upper-mantle heterogeneity, which require array data for proper analysis.

Acknowledgements:

Tianze Liu is supported by a Stanford Graduate Fellowship. We thank all the people who were involved in the deployment of the Peking University temporary array in the Ordos Plateau.

References:

Aki, K., Richards, P.G., 1980. Phase shifts: phase delay and phase advance, in: Quantitative Seismology, Theory and Methods, Volume One. W. H. Freeman and Company, p. 156.

Bao, Y., Niu, F., 2017. Constraining sedimentary structure using frequency dependent P-wave particle motion: a case study of the Songliao Basin in NE China. J. Geophys. Res. Solid Earth. doi:10.1002/2017JB014721

Brocher, T.M., 2005. Empirical relations between elastic wavespeeds and density in the Earth's crust. Bull. Seismol. Soc. Am. 95, 2081–2092. doi:10.1785/0120050077

Christensen, N.I., Mooney, W.D., 1995. Seismic velocity structure and composition of the continental crust: A global view. J. Geophys. Res. Solid Earth 100, 9761–9788. doi:10.1029/95JB00259

Fischer, K.M., Ford, H.A., Abt, D.L., Rychert, C.A., 2010. The Lithosphere-Asthenosphere Boundary. Annu. Rev. Earth Planet. Sci. 38, 551–575. doi:10.1146/annurev-earth-040809-152438

Gao, S., Rudnick, R.L., Xu, W.L., Yuan, H.L., Liu, Y.S., Walker, R.J., Puchtel, I.S., Liu, X., Huang, H., Wang, X.R., Yang, J., 2008. Recycling deep cratonic lithosphere and generation of intraplate magmatism in the North China Craton. Earth Planet. Sci. Lett. 270, 41–53. doi:10.1016/j.epsl.2008.03.008

Griffin, W.L., Andi, Z., O'Reilly, S.Y., Ryan, C.G., 1998. Mantle Dynamics and Plate Interactions in East Asia, in: Flower, M.F.J., Chung, S., Lo, C., Lee, T. (Eds.), Geodynamics Series. American Geophysical Union, Washington, D. C., pp. 107–126. doi:10.1029/GD027

Guan, Z., Niu, F., 2017. An investigation on slowness-weighted CCP stacking and its application to receiver function imaging. Geophys. Res. Lett. 44, 6030–6038. doi:10.1002/2017GL073755

Hauser, E.C., Lundy, J., 1989. COCORP deep reflections: Moho at 50 km (16 S) beneath the Colorado Plateau. J. Geophys. Res. 94, 7071. doi:10.1029/JB094iB06p07071

Kind, R., Kosarev, G.L., Petersen, N. V, 1995. Receiver functions at the stations of the German Regional Seismic Network (GRSN). Geophys. J. Int. 121, 191–202. doi:10.1111/j.1365-246X.1995.tb03520.x

Komatitsch, D., Martin, R., Tromp, J., Taylor, M.A., Wingate, B.A., 2001. Wave propagation in 2-D elastic media using a spectral element method with triangles and quadrangles. J. Comput. Acoust. 9, 703–718. doi:10.1142/S0218396X01000796

Komatitsch, D., Vilotte, J.-P., 1998. The Spectral Element Method : An Efficient Tool to Simulate the Seismic Response of 2D and 3D Geological Structures. Bull. Seismol. Soc. Am. 88, 368–392.

Langston, C.A., 2011. Wave-field continuation and decomposition for passive seismic imaging under deep unconsolidated sediments. Bull. Seismol. Soc. Am. 101, 2176–2190. doi:10.1785/0120100299

Langston, C. a., 1979. Structure under Mount Rainier, Washington, inferred from teleseismic body waves. J. Geophys. Res. 84, 4749. doi:10.1029/JB084iB09p04749

Liu, D.Y., Nutman, A.P., Compston, W., Wu, J.S., Shen, Q.H., 1992. Remnants of Greater-Than-or-Equal-to 3800 Ma Crust in the Chinese Part of the Sino-Korean Craton. Geology 20, 339–342. doi:10.1130/0091-7613(1992)020<0339:romcit>2.3.co;2

Menzies, M. a., Fan, W., Zhang, M., 1993. Palaeozoic and Cenozoic lithoprobes and the loss of >120 km of Archaean lithosphere, Sino-Korean craton, China. Geol. Soc. London, Spec. Publ. 76, 71–81. doi:10.1144/GSL.SP.1993.076.01.04

Owens, T.J., Taylor, S.R., 1984. A Detailed Analysis of Broadband P Waveforms 89, 7783–7795.

Parker, E.H., Hawman, R.B., Fischer, K.M., Wagner, L.S., 2016. Estimating crustal thickness using SsPmp in regions covered by low-velocity sediments: Imaging the Moho beneath the Southeastern Suture of the Appalachian Margin Experiment (SESAME) array, SE Atlantic Coastal Plain. Geophys. Res. Lett. 43, 9627–9635. doi:10.1002/2016GL070103

Randall, G.E., 1989. Efficient calculation of differential seismograms for lithospheric receiver functions. Geophys. J. Int. 99, 469–481. doi:10.1111/j.1365-246X.1989.tb02033.x

Shearer, P.M., 1999. Turning Points and Hilbert Transforms, in: Introduction to Seismology. Cambridge University Press, pp. 106–109.

Shen, W., Ritzwoller, M.H., Schulte-Pelkum, V., 2013. A 3-D model of the crust and uppermost mantle beneath the Central and Western US by joint inversion of receiver functions and surface wave dispersion. J. Geophys. Res. Solid Earth 118, 262–276. doi:10.1029/2012JB009602

Tao, K., Liu, T., Ning, J., Niu, F., 2014. Estimating sedimentary and crustal structure using wavefield continuation: Theory, techniques and applications. Geophys. J. Int. 197, 443–457. doi:10.1093/gji/ggt515

Tromp, J., Komatitsch, D., Liu, Q., 2008. Spectral-element and adjoint methods in seismology. Commun. Comput. Phys. 3, 1–32.

Tseng, T.L., Chen, W.P., Nowack, R.L., 2009. Northward thinning of Tibetan crust revealed by virtual seismic profiles. Geophys. Res. Lett. 36, 1–5. doi:10.1029/2009GL040457

Xia, B., Thybo, H., Artemieva, I.M., 2017. Seismic crustal structure of the North China Craton and surrounding area: Synthesis and analysis. J. Geophys. Res. Solid Earth 5181–5207. doi:10.1002/2016JB013848

Yang, Y., Li, W., Ma, L., 2005. Tectonic and stratigraphic controls of hydrocarbon systems in

the Ordos basin: A multicycle cratonic basin in central China. Am. Assoc. Pet. Geol. Bull. 89, 255–269. doi:10.1360/10070404027

Yu, C., Chen, W.P., van der Hilst, R.D., 2016. Constraints on residual topography and crustal properties in the western United States from virtual deep seismic sounding. J. Geophys. Res. Solid Earth 121, 5917–5930. doi:10.1002/2016JB013046

Yu, C.Q., Chen, W.P., Ning, J.Y., Tao, K., Tseng, T.L., Fang, X.D., John Chen, Y., van der Hilst, R.D., 2012. Thick crust beneath the Ordos plateau: Implications for instability of the North China craton. Earth Planet. Sci. Lett. 357–358, 366–375. doi:10.1016/j.epsl.2012.09.027

Yu, C.Q., Chen, W.P., Van Der Hilst, R.D., 2013. Removing source-side scattering for virtual deep seismic sounding (VDSS). Geophys. J. Int. 195, 1932–1941. doi:10.1093/gji/ggt359

Yu, Y., Song, J., Liu, K.H., Gao, S.S., 2015. Determining crustal structure beneath seismic stations overlying a low-velocity sedimentary layer using receiver functions. J. Geophys. Res. B Solid Earth 3208–3218. doi:10.1002/2014JB011610

Figure 4. *SsPmp* observations from the Ordos plateau, North China. (a): Geometry of the dataset. Triangles: stations. Stars: virtual sources calculated for a crustal thickness of 40 km and V_p = 6.3 km/s. The range of ray parameters (*p*) are for the entire array shown on the map. Yellow triangles and stars correspond to yellow-highlighted traces in (c) and (d). Inset map marks the station map; yellow circles are the epicenters of the two earthquakes. (b) and (c): *Ss* phase from two deep-focus Banda Sea earthquakes recorded by the broadband array shown in (c). Blue and red wiggles: P and S-component waveforms respectively aligned to *Ss* arrival time (0s, picked at the zero-crossing) and normalized by the maximum positive amplitude of *Ss*. Dashed vertical lines separate the two events shown in (c). The traces highlighted with yellow are recorded at yellow triangles in (a). (d-f): Waveforms recorded at JB09, JB13 and FY03. Blue and red: P and S-components waveforms respectively aligned to *Ss* arrival time and normalized by the maximum positive amplitude of *Ss*. Note the ~factor-of-two difference in A_{VDSS} between JB09 and JB13, and the difference in Φ_{VDSS} between JB13 (~90° phase shift from *Ss*) and FY03 (~0° phase shift).

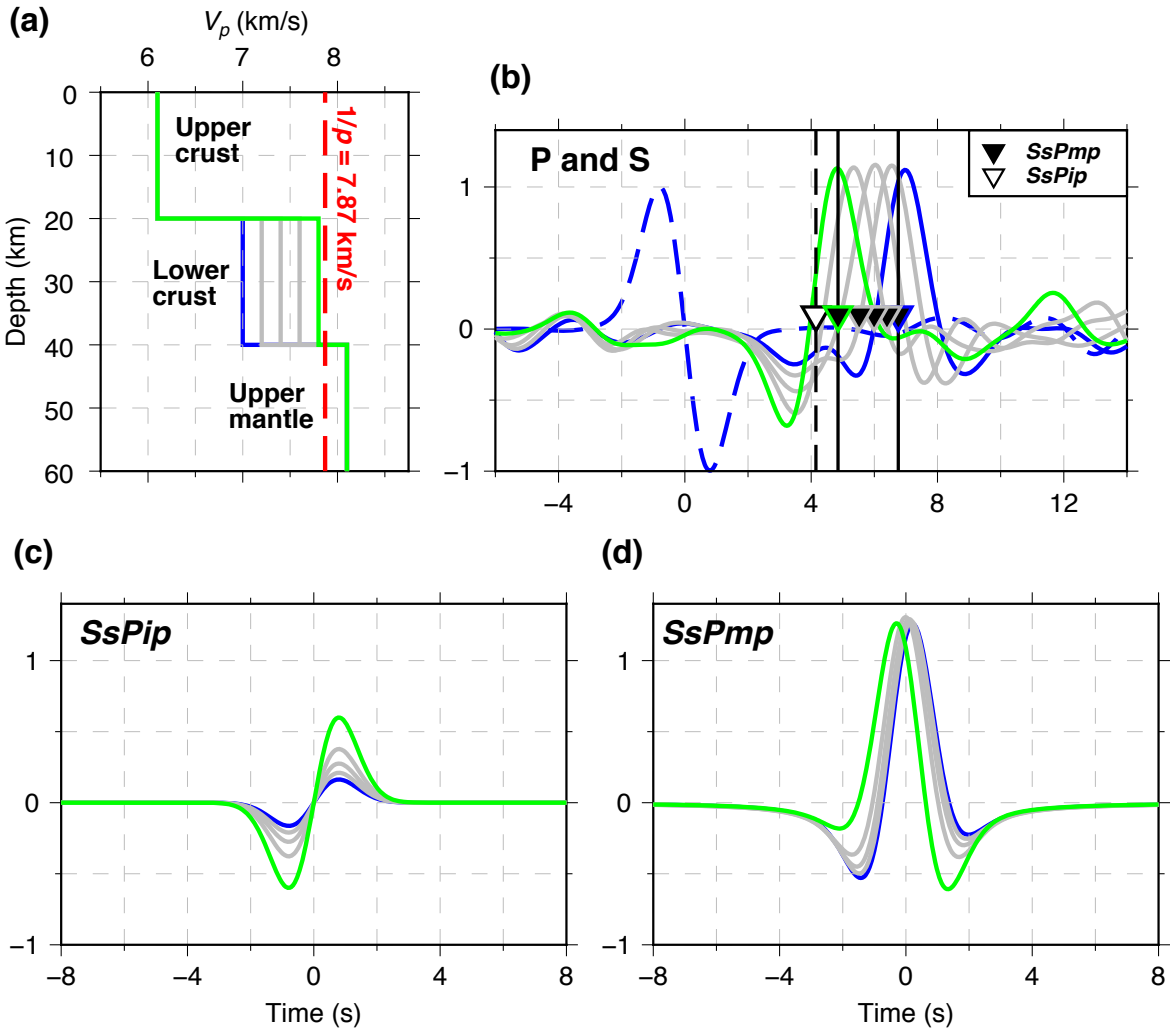

Figure 5. *SsPmp* waveforms computed for ray parameter p = 0.127 s/km and V_p^{lc} ranging from 7.0–7.8 km/s. (a): V_p models used to compute the *SsPmp* synthetic seismograms. Blue: V_p^{lc} = 7.0 km/s. Green: V_p^{lc} = 7.8 km/s. Gray: intermediate models. Red dashed line: critical V_p of incident wave ($1/p$ = 7.87km/s). (b): Blue, gray and green curves: P-component synthetic seismograms colored as in (a). Dashed blue curve: S-component synthetic seismogram computed with V_p^{lc} = 7.0 km/s. Black inverted triangles with blue, gray and green edges: ray-theory-predicted T_{VDSS} of models in (a) colored as in (a). Open inverted triangle: ray-theory-predicted arrival time of the pre-critical reflection phase at the top of the lower crust (*SsPip*), constant for all models. Vertical solid and dashed lines: ray-theory-predicted arrival times of *SsPip* and *SsPmp* (V_p^{lc} = 7.0 and 7.8 km/s). (c) and (d): *SsPip* and *SsPmp* waveforms respectively, colored as in (b), aligned on their ray-theory-predicted arrival times.

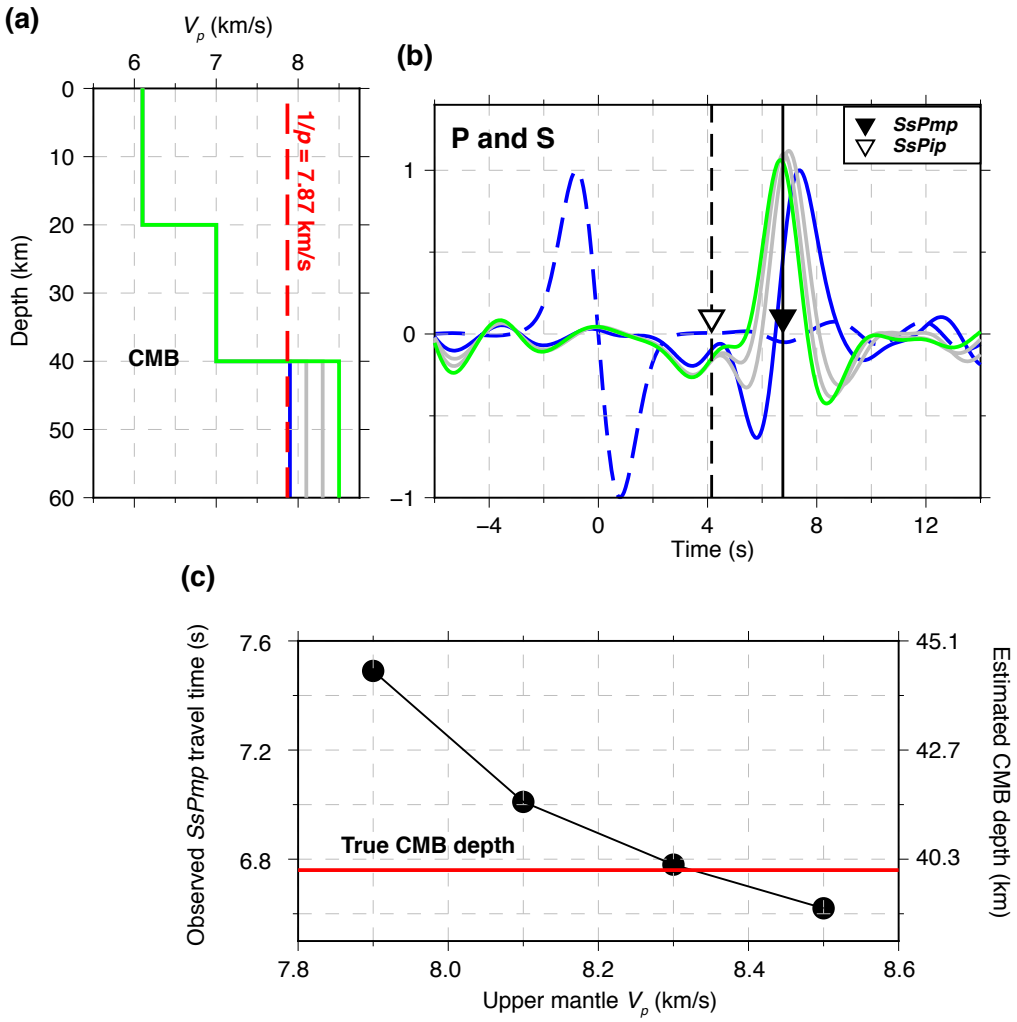

Figure 6. *SsPmp* waveforms for 7.9 ≤ V_p^{um} ≤ 8.5 km/s. (a): V_p models. Blue: V_p^{um} = 7.9 km/s. Green: V_p^{um} = 8.5 km/s. Gray: intermediate models. Red dashed line: critical V_p of the incident wave (1/p =7.87 km/s). (b): Blue, gray and green curves: P-component synthetic seismograms colored as in (a). Dashed blue curve: S-component synthetic seismogram for V_p^{um} = 7.9 km/s. Black (and open) inverted triangles: theoretical T_{VDSS}, (and *SsPip*), constant for all models. (c): Observed T_{VDSS} and estimated Moho depth for waveforms in (b) assuming a 90° phase shift of *SsPmp* relative to *Ss*. The observed T_{VDSS} are found by cross-correlating the 90°-phase-shifted wavelet with the waveforms in (b). The estimated Moho depths are derived from observed T_{VDSS} using Eq. 1 and the true average crustal V_p of the models. Red line: true CMB depth of 40 km.

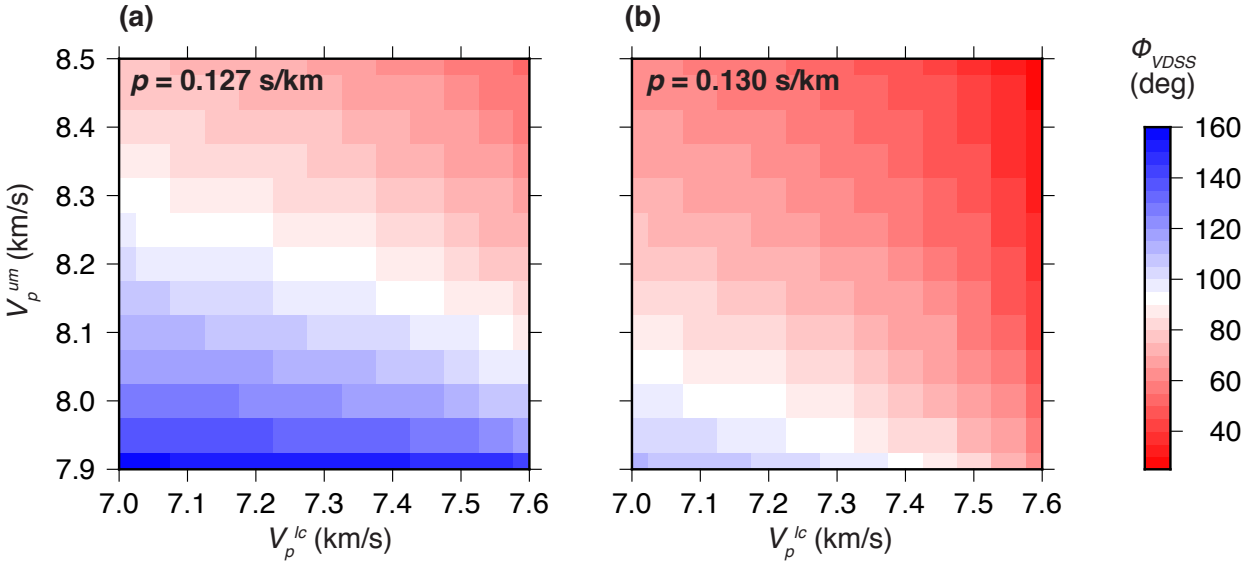

Figure 7. Φ_{VDSS} as a function of V_p^{lc} and V_p^{um} for two different p. The V_s and densities are varied to keep a constant Poisson's Ratio of 0.25, and to satisfy the Nafe-Drake relation (Brocher, 2005). (a) Φ_{VDSS} as a function of V_p^{lc} and V_p^{um} when p = 0.127 s/km. (b) Φ_{VDSS} as a function of V_p^{lc} and V_p^{um} when p = 0.130 s/km. Note that when p = 0.127 s/km Φ_{VDSS} is primarily controlled by V_p^{um}, whereas when p = 0.130 s/km Φ_{VDSS} is affected by both V_p^{lc} and V_p^{um}.

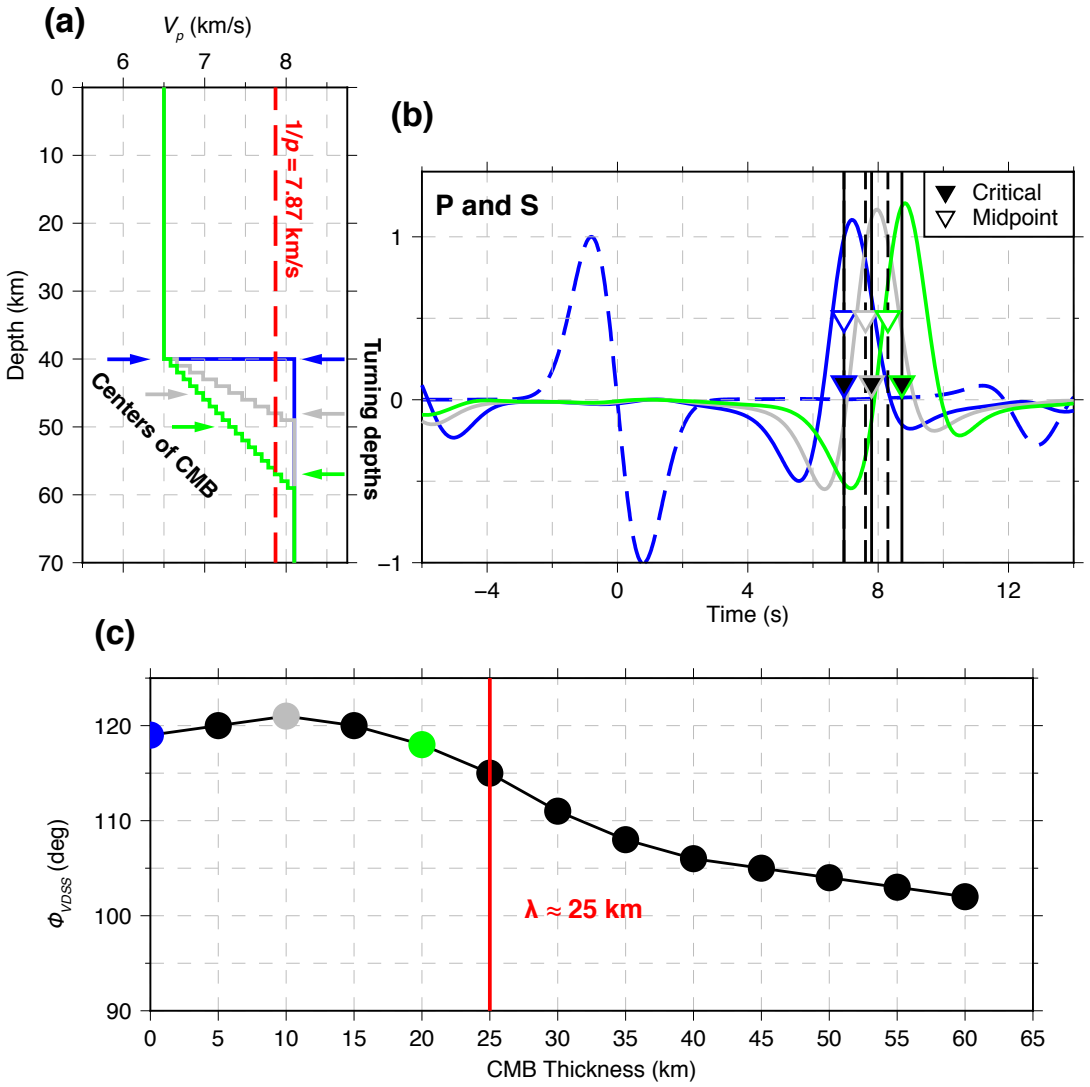

Figure 8. *SsPmp* waveforms for a CMB thickness of 0 (velocity discontinuity), 10 and 20 km. (a) V_p models. Blue: CMB as a velocity discontinuity at 40-km depth. Grey: 10-km thick CMB. Green: 20-km thick CMB. Red dashed line: critical V_p of the incident wave ($1/p$ = 7.87 km/s). (b) Blue, grey and green curves: P-component synthetic seismograms colored as in (a). Dashed blue curve: S-component synthetic seismogram computed with the discontinuous CMB model plotted for reference. Black inverted triangles with blue, grey and green edges: theoretical T_{VDSS} of the models colored as in (a), calculated for the depths at which V_p = 7.87 km/s, i.e. at which V_p equals the critical velocity (the reciprocal ray parameter). Open inverted triangles with blue, grey and green edges: theoretical T_{VDSS} of the models colored as in (a), calculated for the depths to the center of the CMB. (c) Φ_{VDSS} as a function of CMB thickness. V_p at the top and bottom of the CMB are fixed at 6.5 and 8.1 km/s. Blue, gray and green circles: models colored as in (a). Red line: dominant wavelength λ of P waves with dominant frequency 0.25 Hz in the CMB. Note that as CMB thickness becomes larger than λ, Φ_{VDSS} deviates significantly from the value with a velocity discontinuity.

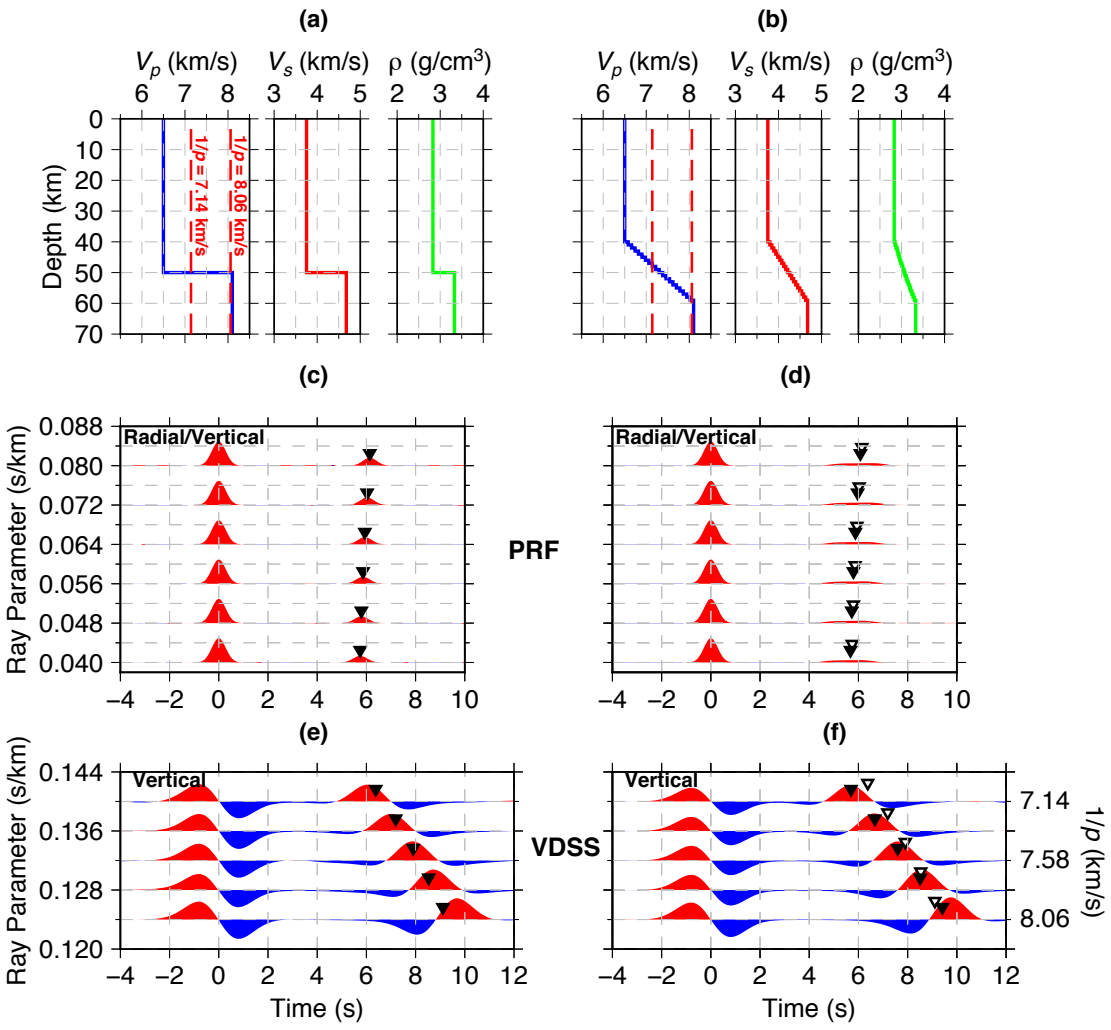

Figure 9. Synthetic RF and *SsPmp* waveforms with different ray parameters for different CMB thicknesses but the same total velocity change across the CMB. (a) and (b): 1D Models in which the CMB is represented by either a discontinuity in V_p, V_s and density, or by a 20-km thick transition zone. (c) and (d): Synthetic PRFs (radial components deconvolved by vertical components) computed with the models in (a) and (b), respectively, and ray parameters ranging from 0.04-0.08 s/km. Black inverted triangles are theoretical *Pms* travel times for a conversion depth at 50 km, i.e. at the abrupt discontinuity (model a) or at the center of the transition zone (model b). Open triangles in (d) show the theoretical arrival times in model a, offset vertically to be visible. (e) and (f): Vertical-component synthetic *SsPmp* waveforms computed with model a and b respectively, and ray parameters ranging from 0.124-0.140 s/km. The corresponding turning velocities ($1/p$) are labeled on the right. Black inverted triangles in (e) are theoretical T_{VDSS} for reflections at the discontinuity, and in (f) are theoretical T_{VDSS} computed for reflections at the depth where $V_p = 1/p$. Open inverted triangles in (f) show T_{VDSS} in (e), offset vertically to be visible. Note that theoretical T_{VDSS} in (e) and (f) form distinct move-out curves with respect to p, and that Φ_{VDSS} varies with p

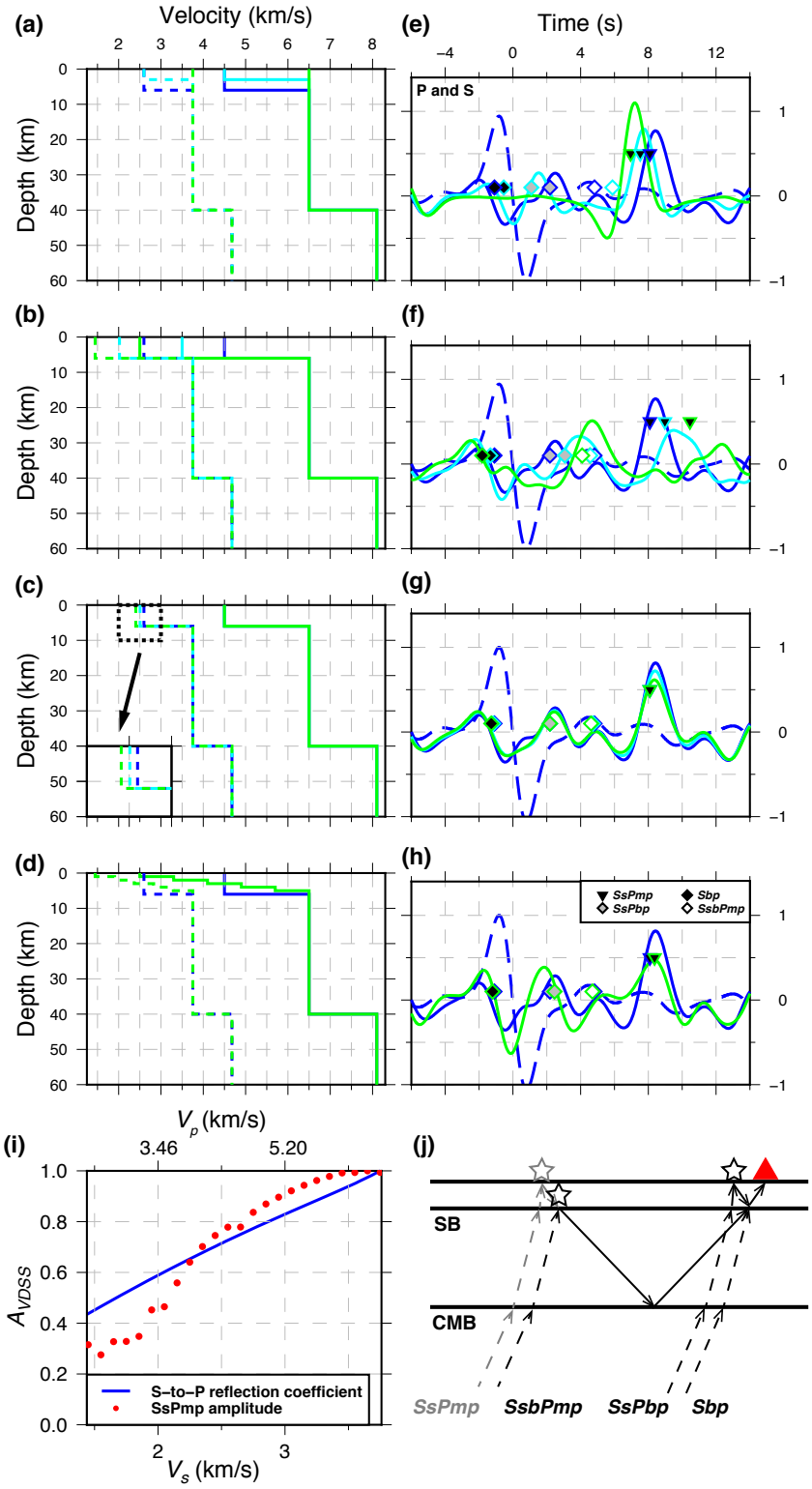

Figure 10. *SsPmp* waveforms for different sedimentary basins on top of the same crust with 40-km-deep Moho. (a), (b), (c) and (d): V_p (solid lines) and V_s (dashed lines) models of simple sedimentary basins. Blue lines in each part: our 'standard model', a 6-km thick sedimentary layer (V_p = 4.5km/s) above basement (V_p = 6.5km/s) and a CMB discontinuity at 40 km depth above V_p^{um} = 8.1 km/s; Poisson's ratio = 0.25. In (a) we vary sedimentary thickness between 6 km (blue), 3 km (cyan), and 0 km (no sedimentary layer, green). In (b) we vary sedimentary V_p between 4.5 km/s (blue), 3.5 km/s (cyan) and 2.5km/s (green); V_s is also varied to keep Poisson's ratio at 0.25. In (c) we vary sedimentary Poisson's ratio between 0.25 (blue), 0.275 (cyan), and 0.3 (green), while keeping the sedimentary V_p at 4.5 km/s (The inset figure shows the zoom-in plot of V_s in the basin). In (d), we vary the velocity gradient in the sedimentary basin between a constant velocity (blue) and a stack of six 1-km thick layers with V_p linearly increasing with depth from 1.5-6.5km/s (green). (e), (f), (g), and (h): Solid curves: P-component synthetic seismograms for velocity models (a), (b), (c) and (d) respectively, and colored as in these velocity models. Dashed blue curves: S-component synthetic seismograms for standard model. Black inverted triangles with edges colored corresponding to the velocity models mark theoretical T_{VDSS}. Black, gray and white diamonds with edges colored corresponding to the velocity models mark theoretical arrival times of *Sbp*, *SsPbp*, and *SsbPmp* . (i): Effects of sedimentary basin on A_{VDSS}. Red circles: maximum amplitude in a 4-s time window around the theoretical T_{VDSS} as a proxy for A_{VDSS} for models with sedimentary V_s ranging from 1.45-3.75 km/s (basin thickness and Poisson's ratio are fixed at 6 km and 0.25). Blue curve: S-to-P reflection ratio at the free surface for a half-space (i.e. no basin) for the same V_s range and Poisson's ratio = 0.25. Both the red circles and blue curve are normalized with their maximum values for the convenience of plotting. The corresponding sedimentary V_p are plotted on the top. (j): Ray paths of *SsPmp, Sbp, SsPbp and SsbPmp*.

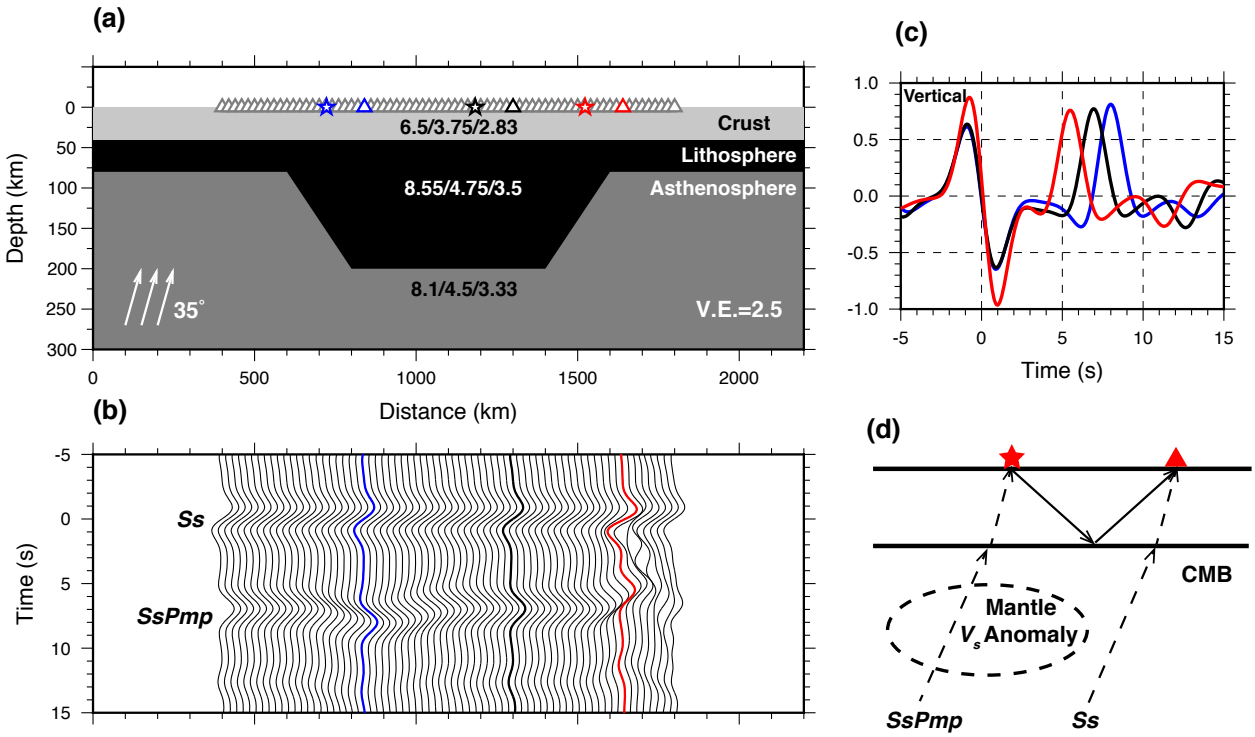

Figure 11. Effects of lateral variation in mantle V_s on T_{VDSS}. (a): 2D model used to compute synthetic seismograms, with a vertical exaggeration of 2.5. Light gray: crust. Black: lithospheric mantle. Dark gray: asthenosphere. Material properties of model layers are listed as V_p (km/s)/V_s (km/s)/ρ (g/cm^3). Incident angle of the plane S wave is 35°, and the dip of the lithosphere-asthenosphere boundary is 31°. The seismograms of the stations highlighted with blue, black and red are shown in (b) and (c). Stars show the virtual sources of the stations highlighted with the same colors. (b): Vertical-component synthetic seismograms recorded by stations in (a). Black, blue and red traces: traces recorded by highlighted stations in (a) and colored accordingly. Note the significant lateral variation of T_{VDSS} despite homogeneous crustal thickness. (c): Vertical-component synthetic seismograms recorded by highlighted stations in (a) and colored accordingly. (d): Schematic showing V_s anomaly in the mantle affects T_{VDSS} by changing the relative travel times of *Ss* and the S legs of *SsPmp*.

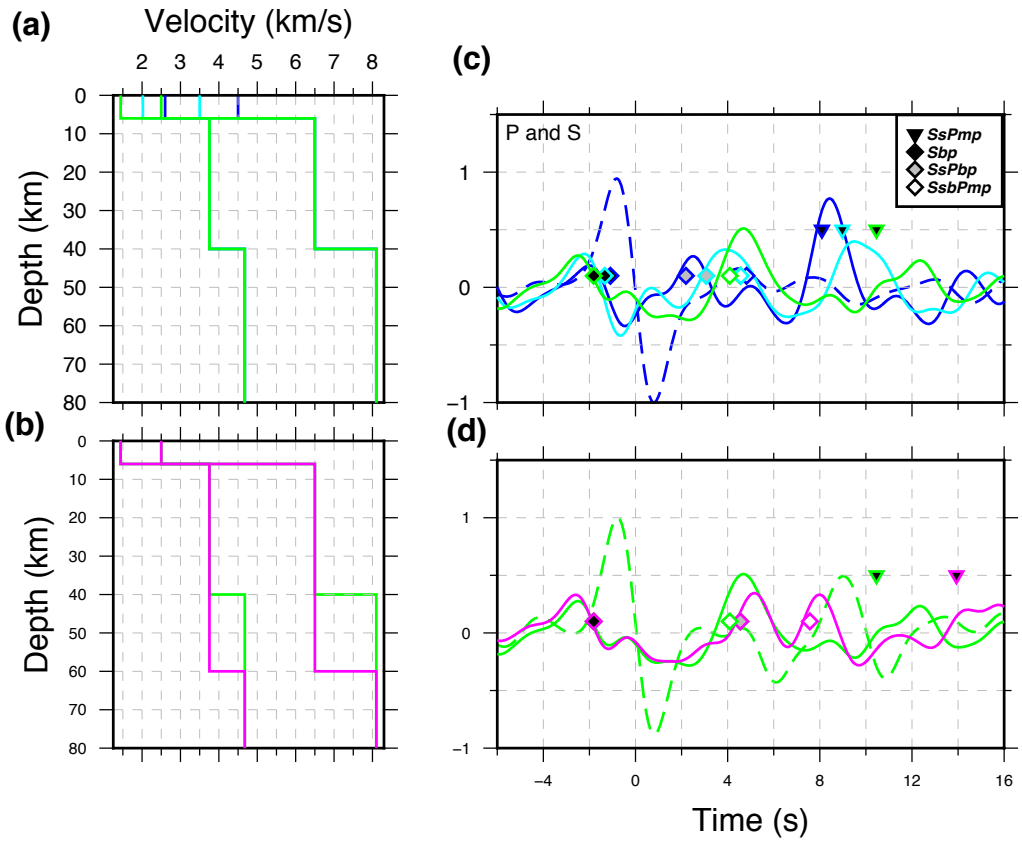

Figure S1. (a): The same as Fig. 8b. (b): V_p and V_s models with the same sedimentary layer thickness (6 km), V_p (4.5 km/s) and Poisson's ratio (0.25), but with Moho thickness varied between 40 km (green curve) and 60 km (magenta curve). The green model is the same as the green one in (a). (c): The same as Fig. 8f. (d): Solid curves: P-component synthetic waveforms calculated from velocity models in (b) and colored as in (b). Dashed green curves: S-component synthetic seismograms computed with the green model in (b).